Oscillations, travelling fronts and patterns in a supramolecular system

Jorge Leira Iglesias, Alessandra Tassoni, Takuji Adachi, Michael Stich, Thomas M. Hermans

Oscillations, traveling fronts and patterns in a supramolecular system

Jorge Leira-Iglesias[1], Alessandra Tassoni[1], Takuji Adachi[1], Michael Stich[2] and Thomas M. Hermans[1]*

1 University of Strasbourg, CNRS, ISIS UMR 7006, F-67000 Strasbourg, France

2 Non-linearity and Complexity Research Group, Systems Analytics Research Institute, Engineering and Applied Science, Aston Triangle, Birmingham B4 7ET, United Kingdom.

* hermans@unistra.fr

Supramolecular polymers such as microtubules operate under non-equilibrium conditions to drive crucial functions in cells such as motility, division and organelle transport.[1] In vivo and in vitro size oscillations of individual microtubules[2,3] (dynamic instabilities) and collective oscillations[4] have been observed. In addition, dynamic spatial structures like waves and polygons can form in non-stirred systems.[5] Here we describe an artificial supramolecular polymer made of a perylene diimide derivative that displays oscillations, traveling fronts, and centimetre-scale self-organized patterns when pushed far from equilibrium by chemical fuels. Oscillations arise from a positive feedback due to nucleation-elongation-fragmentation, and a negative feedback due to size-dependent depolymerisation. Traveling fronts and patterns form due to self-assembly induced density differences that cause system-wide convection. In our system, the species responsible for the non-linear dynamics and those that self-assemble are one and the same. In contrast, other reported oscillating assemblies formed by vesicles[6], micelles[7], or particles[8] rely on the combination of a known chemical oscillator and a stimuli-responsive system, either by communication through the solvent (e.g., by changing pH[7–9]), or by anchoring one of the species covalently (e.g., Belousov-Zhabotinsky catalyst[6,10]). Designing self-oscillating supramolecular polymers and large scale dissipative structures bring us closer to create more life-like materials[11] that respond to external stimuli similarly to living cells, or to create artificial autonomous chemical robots.[12]

We use a perylene diimide derivative **PDI** that forms supramolecular polymers in aqueous borate buffer (Figure 1a). Upon reduction by $Na_2S_2O_4$ the dianion $\mathbf{PDI^{2-}}$ is mostly monomeric, and at equilibrium with small ~100 nm $\mathbf{PDI^{2-}}$ assemblies (see below).[13] Oxidation by atmospheric oxygen leads first to the radical anion $\mathbf{PDI^{\bullet-}}$, before returning to the neutral $\mathbf{PDI_{mon}}$ (see Methods). The latter undergoes a cooperative supramolecular polymerisation to form micron-sized colloidal assemblies $\mathbf{PDI_{assem}}$ by side-to-side bundling of one-dimensional **PDI** fibers.[13] The polymerisation process can be followed by UV-Vis spectroscopy where a characteristic band at 528 nm can be tracked, colour camera where pink / blue / purple corresponds to **PDI** / $\mathbf{PDI^{\bullet-}}$ / $\mathbf{PDI^{2-}}$ respectively, or dynamic light scattering (Supplementary Figures 1 and 2).

The cooperative nature of the assembly process is discerned from the sigmoidal time progression of the degree of polymerisation α vs. time (Figure 1c), where α = 0 corresponds to the disassembled state and α = 1 to the fully assembled state. Light scattering shows a similar sigmoidal increase from ~100 to 1500 nm in hydrodynamic radius R_H during assembly (Supplementary Figure 3, black line). In addition, the fact that the half-time τ scales as $\log(\tau) \propto -0.48 \log(C_0)$, where C_0 is the initial concentration of **PDI**, indicates that more processes are occurring than only nucleation and elongation (Supplementary Section 2 and Supplementary Figure 4). A detailed analysis including seeding experiment and global fitting by analytical models[14] showed that fragmentation is also involved (Figure 1c, Supplementary Section 2). Fragmentation was further confirmed by performing experiments at different stirring / shear rates, where the fastest growth was observed at the highest rate (cf. Supplementary Figure 7). Others have shown that stirring can lead to fragmentation[15] or increased secondary nucleation[16].

The reduction rate of $\mathbf{PDI_{assem}}$ was quantified using stopped-flow experiments, where a solution of reductant $Na_2S_2O_4$ was rapidly mixed with $\mathbf{PDI_{mon}}$ solutions that had been aged for determined times. Solutions prepared from freshly synthesized **PDI** powder gave seemingly random reduction kinetic profiles, due to the broad distribution[13] of particle sizes. Therefore, all solutions were first fully reduced to $\mathbf{PDI^{2-}}$, and stirred in air until a bright pink colour of the neutral $\mathbf{PDI_{mon}}$ was observed. The latter solution was rapidly transferred into the stopped-flow syringe and left to age. Figure 1d shows a typical reduction experiment tracked using the $\mathbf{PDI^{2-}}$ absorption

band at 612 nm, which shows first a fast exponential increase up to ~1 s, followed by a slower sigmoidal increase. These complicated kinetics can be understood by a 2-step process: 1) a first-order reaction where $Na_2S_2O_4$ reacts with the outer shell of the **PDI$_{assem}$** colloidal assemblies leading to a rapid colour / absorption change (i in Fig. 1b), and 2) surface-erosion of the colloids leading to sigmoidal release[17] of **PDI** into solution followed by instantaneous reduction to **PDI^{2-}** (ii–iv in Fig. 1b). The time constants corresponding to these two processes (τ_1 and τ_2, respectively) both increase by a factor 2–3 over the 90 min aging period (cf. insets in Figure 1d). In other words, during the **PDI$_{mon}$** to **PDI$_{assem}$** aging the assemblies are getting larger and larger (from ~100 nm to ~2 µm, cf. Supplementary Section 1), leading to ever slower apparent reduction rates.

So far, we have shown that there is significant non-linearity in both the assembly and disassembly kinetics of **PDI** structures. The nucleation-elongation-fragmentation process acts as a positive feedback mechanism, whereas the size-dependent reduction / disassembly of **PDI** can be seen as a negative feedback; both of which are thought to be required[18] to obtain emergent properties such as oscillations. With the basic elements to construct an oscillator in place we set out to find the oscillating window by pushing the system far from equilibrium in a stirred semi-batch reactor.

Practically, we placed a stirred glass vial in a well-ventilated box with constant oxygen supply and illumination and used a syringe pump to inject the reductant ($Na_2S_2O_4$) solution continuously (Figure 2a). A fast diode-array UV/Vis detector, colour CCD camera, near infra-red static light scattering IR-SLS, and confocal microscopy were used for analysis (Supplementary Section 3 and 4). Conventional visible light scattering cannot be used, since 1) **PDI^{2-}** absorbs the 639 nm laser light, preventing quantitative static light scattering (cf. Supplementary Figure 3), and 2) stirring disrupts the correlation needed for dynamic light scattering. A home-built 905 nm IR-SLS setup was used instead (Supplementary Figure 9); to benchmark the setup we performed a step-wise redox cycle (Supplementary Figure 10), namely: i) a solution of **PDI$_{assem}$** has significant IR-SLS intensity and a pink colour, ii) addition of reductant leads to **PDI^{2-}** and a fast drop of the colour intensity of the red and blue channel, iii) oxidation in air to **PDI$^{\bullet-}$** results in a local maximum in blue intensity, iv) further oxidation to **PDI$_{mon}$** restores the initial pink solution colour while the IR-SLS intensity reaches a minimum, v) assembly into **PDI$_{assem}$** leads to a sigmoidal increase in scattering and visual turbidity. The latter experiment shows that reduction leads to disassembly and low IR-SLS intensity, and that **PDI$_{mon}$** is the least assembled state consisting of ~100 nm structures.

The phase space of the system was explored in the semi-batch reactor by varying the initial concentration of **PDI** vs. the flow rate of reductant (Figure 2b). In all cases, the initial solution was completely reduced to **PDI^{2-}** before starting the continuous inflow of reductant. The composition of the solution species **PDI^{2-}** / **PDI$^{\bullet-}$** / **PDI$_{mon}$** / **PDI$_{assem}$** was determined from colour analysis and UV/Vis spectra (see supplementary section 3). For low flow rates a steady state 'SS' was observed by following the red channel of the CCD camera (Figure 2b,c). The composition of the solution is close to fully neutral assembled **PDI**, apparent from the solution colour and UV-Vis spectrum. To confirm the latter, the reductant inflow was stopped, causing full oxidation and assembly into **PDI$_{assem}$**, and leading only to a minor (< 5 %) increase in intensity (Supplementary Figure 11a). Increasing the flow rate further, leads to complex oscillations in a narrow window 'OSC' (Figure 2b,d, Supplementary Video 1). For the highest flow rates, precipitation 'PR' occurred after ~40 min, where a film of solids would accumulate at the solution/air interface (Figure 2b,e).

Oscillations were always damped and with seemingly period-2 characteristics. That is, oscillations occur in 'pairs', where one of the two peaks is lower than the other (cf. Figure 2d). The amplitude of the oscillations gradually decreases, whereas their frequency is ever increasing. The path to oscillations can be understood by looking at the colour space in two-dimensions (Figure 2f). To this end, the red / green / blue channels obtained from the camera are converted to CIE 1931 x and y colour coordinates. In Figure 2f the process is as follows: i) reduction of **PDI** solution to **PDI^{2-}** by addition of an aliquot of $Na_2S_2O_4$ solution; ii) atmospheric air oxidizes to **PDI$^{\bullet-}$** until very small **PDI$_{mon}$** structures are formed; iii) sigmoidal growth to large assemblies **PDI$_{assem}$**; iv) start of the continuous flow of reductant, followed shortly by oscillations; v) damping and decay of oscillations. To be sure that oscillations in the size of the assemblies occurred, we performed experiments combining IR-SLS with colour tracking (Figure 2g and Supplementary Figure 12). In Figure 2g one can see that during a large oscillation all the way to disassembled **PDI^{2-}** (index ii), the IR-SLS intensity drops to the baseline and the (red) colour intensity is low as well; shortly thereafter, neutral **PDI$_{mon}$** is formed (index iii) leading to rapid increase in colour intensity, followed by a much slower sigmoidal increase in IR-SLS intensity and visual turbidity in the vial (index iv).

A subsequent oscillation shows a similar trend (cf. indices v–viii in Figure 2g). Further evidence comes from confocal microscopy, where aliquots were taken during oscillations showing nearly complete disappearance of colloidal assemblies during large oscillations (e.g., compare v and vi in Supplementary Figure 13).

In general, many oscillators studied under semi-batch conditions show damped oscillations due to accumulation of waste products. Microtubules for example, suffer from increasing concentrations of guanosine diphosphate over their triphosphate analogue, which is thought to lead to amplitude loss in batch experiments.[20,21] To test whether waste accumulation was of importance in our system, we added an equivalent of 5 hours of waste mid-way during oscillations (Supplementary Figure 14a). Only a very minor disturbance in the oscillations was observed. As a negative control, an aliquot of buffer of the same volume as in the 'waste addition experiments' was added, which did not disturb the oscillations (Supplementary Figure 14b). From the latter two series of experiments we conclude that waste accumulation or resulting changes in ionic strength are not responsible for the damping of the oscillations. Another salient detail is that oscillations can never be obtained when starting from aged $\mathbf{PDI_{assem}}$ solutions, but only when starting from mostly disassembled $\mathbf{PDI_{mon}}$ solutions (i.e., by fully reducing to $\mathbf{PDI^{2-}}$, and then oxidizing to **PDI** before starting inflow of reductant). In other words, the oscillations are inherently transient and 'en route' to a non-oscillating state consisting of large $\mathbf{PDI_{assem}}$. The latter is also confirmed by the model we develop (see below).

To understand the oscillator behaviour, we expanded a recent nucleation-elongation-fragmentation model[19] (used above, cf. Figure 1c) with chemically-fuelled reduction by $Na_2S_2O_4$ and oxidation by O_2. Specifically, we consider reduction of a polymer Q_j of length j (i.e., the removal of an end-capped monomer from a one-dimensional polymer and its instantaneous reduction), and oxidation of non-assembled reduced monomer R to monomer O. Since both $\mathbf{PDI^{\bullet-}}$ and $\mathbf{PDI^{2-}}$ are mostly disassembled (cf. Supplementary Figure 2), we combine them both into reduced monomer R. Figure 3a shows the used equations, rate constants, and schematic representations of the model. Using the mathematical approach by Knowles and co-workers[19] we derived the following equations (cf. Supplementary section 5) for the number concentration of polymers [P], the mass concentration of polymers [M], and the concentrations [O] and [R] of the monomer species:

$$\frac{d[P]}{dt} = -3k_{frag}[P] + k_{frag}[M] + k_{nuc}[O]^2, \quad (1)$$

$$\frac{d[M]}{dt} = -2\left(k_{frag} + k_{red}\right)[P] + 2k_{el}[P][O] + 2k_{nuc}\,[O]^2, \quad (2)$$

$$\frac{d[R]}{dt} = k_{red}[P] - k_{ox}[R], \quad (3)$$

$$[O] = [m]_{tot} - [M] - [R], \quad (4)$$

where we have used nucleus size $n = 2$ and conserve the total mass $[m]_{tot}$. A continuation analysis and simulations of the model were performed with MatCont (see Supplementary Section 5). The main finding is that damped oscillations can be observed in all variables (total number of polymers, total mass of polymers, and the monomer concentrations) for an extended range of parameters (cf. Figure 3b and Supplementary Figure 15). We classify the behaviour as oscillating if the amplitude within 3 consecutive oscillations is larger than 50% of the asymptotic steady state value of [M]. A number of aspects of the model are in qualitative agreement with the experiments. One can compare Figure 3b to 2b (see above), where in the former at low flow rate of reductant a steady-state SS is obtained, and in the latter analogously at low k_{red} a SS is found (note: k_{ox} in the experiments is always constant, and determined by influx of atmospheric oxygen). In other words, at low rates of reduction the molecules stay in the assembled $\mathbf{PDI_{assem}}$ state, as one would expect. Increasing k_{red} values leads to damped oscillations (OSC in Figure 3b), since there is a competition between assembled and disassembled **PDI** with non-linear kinetics. The top inset in Figure 3b shows time traces along a vertical phase line, where decreasing k_{ox} leads to more oscillations (i.e., less damping), an increasing asymptotic value, and an increasing period. A similar trend is seen for the horizontal phase line (bottom inset Figure 3b) in the direction of increasing k_{red} at constant k_{ox}. For too large k_{red} the oscillations become unstable and lead to unphysical (negative and extremely large) concentrations, shown in the 'US' region in Figure 3b. Surprisingly, this is where in experiments precipitation is observed (Figure 2b), though a direct comparison cannot be made at this point.

Other than the chemically fuelled rates constants k_{ox} and k_{red}, fragmentation k_{frag} is a sensitive parameter; decreasing its value leads to a decrease in damping (Figure 3c), allowing hundreds of oscillations up to the point that experimentally it would be difficult to distinguish from

sustained oscillations. More generally, we can vary the nucleation k_{nuc}, and elongation k_{el} rates and conserve the qualitative finding—that is, the oscillations are generic. If the initial condition contains enough polymers, the nucleation rate can even be set to zero, while maintaining the oscillations.

Beyond oscillations, we investigated the spatiotemporal behaviour of our supramolecular system. Firstly, we explored traveling fronts, where a **PDI$_{mon}$** solution was seeded with preformed 1h old **PDI$_{assem}$** polymers, leading to isothermal frontal supramolecular polymerisation in adjacent volumes (Figure 4a,b, and Supplementary Video 2). Temperature differences are not important in our system as they would quickly equalize due to fast thermal diffusion.[22] In a rectangular chip with two parallel glass slides spaced by 1 mm, a traveling front with an initial velocity of 0.26 ± 0.01 mm min^{-1}—about ~20 times faster than ~100 nm **PDI$_{mon}$** diffusion—can be seen that increases the area initially occupied by the seeds (cf. left panel of Figure 4b and Supplementary Video 2). Later on, a ring structure is formed that slows down progressively until it stops completely, as can be seen in the kymograph in Figure 4c. Upon closer inspection of the traveling front using confocal microscopy and analysis by particle image velocimetry, it was clear that large scale in-plane convection was present in the chip, shortly after seeds were added (Supplementary Video 3). As a control, we added **PDI$_{assem}$** and buffer to the same **PDI$_{mon}$** solution, and observed much more spreading of the seeded front vs. the non-seeded region (Supplementary Video 4). In other words, seeding triggers the convective front, similarly to (thermal) initiation in covalent frontal polymerisation.[23] **PDI$_{mon}$** solutions have an ~0.2% higher density as compared to fully assembled **PDI$_{assem}$** (Supplementary Figure 16). While this seems like a small difference, it is known that in a horizontal experiment, neighbouring volumes with different density always lead to convective instabilities.[22] The traveling front progressively slows down (Figure 4c), since spontaneous nucleation and growth occurs in the unreacted zones over time as well, reducing the density difference with the front, and thus halting convection.

When replacing the top glass plate with mineral oil, convection is exacerbated and a single massive convection cell is formed (Figure 4d). In the latter experiment, **PDI^{2-}** is oxidized by atmospheric oxygen diffusing through the oil, leading to an outward moving propagating oxidation front (cf. dashed area, Figure 4d), while simultaneously turning the entire volume into a single convection cell leading to alignment of **PDI$_{assem}$** structures along the flow lines (Supplementary Video 5). Small scale convection is observed in unseeded as well as seeded experiments (far from the front), where mosaic structures are formed (Figure 4e and Supplementary Figure 17). Similar structures have been observed in microtubule experiments[5] and in an inorganic system[24]. Again, spontaneous nucleation and growth leads to small zones of different composition and density, inducing localized structures.

We have shown collective size oscillations in a supramolecular polymer system by combining cooperative self-assembly with chemically fuelled disassembly. Interestingly, our model shows that non-linear negative feedback like we have observed experimentally (i.e., size-dependent reduction / disassembly rates, see above) is not required; positive non-linear feedback from the supramolecular polymerisation combined with chemically-fuelled linear depolymerisation is sufficient to obtain oscillations. This provides an exciting outlook for other supramolecular polymers reported on so far,[25–29] which use chemical fuels to drive (seemingly) cooperative polymerisation. The type of supramolecular oscillations we find here are always damped. This is because they are found close to a subcritical Hopf bifurcation,[30] which leads to an unstable limit cycle and therefore does not support sustained oscillations. Similar observations have been made in microtubule systems, where inherent damping was suggested as well.[31] Other than temporal order, we have shown spatiotemporal phenomena. In non-stirred experiments cm-scale polymerization fronts and polygonal convection patterns are formed due to density differences between assembled and non-assembled regions. The latter polygons are *dissipative structures* in the Prigogine-sense, meaning they are only observed beyond stability of the thermodynamic branch.[32] Recognizing dissipative structures in supramolecular systems is difficult, since order can already exists at equilibrium due to non-covalent interactions. Dissipative structures, however, occur at length-scales much larger than the molecules and their fundamental (intermolecular) interactions, and should disappear if the system were to be isolated. Our system has nm–μm scale order at the level of the supramolecular structures, as well as cm-scale order at the level of the dissipative (convective) structures. It will be interesting to further explore the interplay of out-of-equilibrium supramolecular polymerisation with convective instabilities, in addition to recent enzymatic convection patterns[33] and supramolecular–mechanical couplings[34,35]. This will allow large scale self-organization, transport, and communication driven by fuelled dissipative non-equilibrium self-assembly[36]. In general, non-equilibrium supramolecular

polymerization[36,37] only leads to large scale emergent properties such as oscillations when the system is pushed far from equilibrium beyond the first bifurcation.

Data availability. The data that support the plots within this paper and other findings of this study are available from the corresponding authors upon reasonable request.

References

1. Alberts, B. *et al. Molecular Biology of the Cell*. (Garland Science, 2002).
2. Valiron, O., Caudron, N. & Job, D. Microtubule dynamics. *Cell. Mol. Life Sci. CMLS* **58,** 2069–2084 (2001).
3. Mandelkow, E.-M. & Mandelkow, E. Microtubule oscillations. *Cell Motil. Cytoskeleton* **22,** 235–244 (1992).
4. Houchmandzadeh, B. & Vallade, M. Collective oscillations in microtubule growth. *Phys. Rev. E* **53,** 6320 (1996).
5. Mandelkow, E., Mandelkow, E. M., Hotani, H., Hess, B. & Muller, S. C. Spatial patterns from oscillating microtubules. *Science* **246,** 1291–1293 (1989).
6. Tamate, R., Ueki, T., Shibayama, M. & Yoshida, R. Autonomous unimer-vesicle oscillation by totally synthetic diblock copolymers: effect of block length and polymer concentration on spatio-temporal structures. *Soft Matter* **13,** 4559–4568 (2017).
7. Lagzi, I., Wang, D., Kowalczyk, B. & Grzybowski, B. A. Vesicle-to-Micelle Oscillations and Spatial Patterns. *Langmuir* **26,** 13770–13772 (2010).
8. Lagzi, I., Kowalczyk, B., Wang, D. & Grzybowski, B. A. Nanoparticle Oscillations and Fronts. *Angew. Chem. Int. Ed.* **49,** 8616–8619 (2010).
9. Wang, G. *et al.* The non-equilibrium self-assembly of amphiphilic block copolymers driven by a pH oscillator. *Colloids Surf. Physicochem. Eng. Asp.* **529,** 808–814 (2017).
10. Yoshida, R. Self-Oscillating Gels Driven by the Belousov–Zhabotinsky Reaction as Novel Smart Materials. *Adv. Mater.* **22,** 3463–3483 (2010).
11. Grzybowski, B. A. & Huck, W. T. S. The nanotechnology of life-inspired systems. *Nat. Nanotechnol.* **11,** 585–592 (2016).
12. Hess, H. & Ross, J. L. Non-equilibrium assembly of microtubules: from molecules to autonomous chemical robots. *Chem. Soc. Rev.* **46,** 5570–5587 (2017).
13. Leira-Iglesias, J., Sorrenti, A., Sato, A., Dunne, P. A. & Hermans, T. M. Supramolecular pathway selection of perylenediimides mediated by chemical fuels. *Chem Commun* **52,** 9009–9012 (2016).
14. Meisl, G. *et al.* Molecular mechanisms of protein aggregation from global fitting of kinetic models. *Nat. Protoc.* **11,** 252–272 (2016).
15. Carnall, J. M. A. *et al.* Mechanosensitive Self-Replication Driven by Self-Organization. *Science* **327,** 1502–1506 (2010).
16. Kondepudi, D. K. & Sabanayagam, C. Secondary nucleation that leads to chiral symmetry breaking in stirred crystallization. *Chem. Phys. Lett.* **217,** 364–368 (1994).
17. Ulery, B. D., Nair, L. S. & Laurencin, C. T. Biomedical applications of biodegradable polymers. *J. Polym. Sci. Part B Polym. Phys.* **49,** 832–864 (2011).
18. Scott, S. K. *Oscillations, Waves, and Chaos in Chemical Kinetics*. (Oxford University Press, Incorporated, 1994).
19. Cohen, S. I. A. *et al.* Nucleated polymerization with secondary pathways. I. Time evolution of the principal moments. *J. Chem. Phys.* **135,** 065105 (2011).
20. Sept, D., Limbach, H. J., Bolterauer, H. & Tuszynski, J. A. A Chemical Kinetics Model for Microtubule Oscillations. *J. Theor. Biol.* **197,** 77–88 (1999).
21. Lange, G., Mandelkow, E.-M., Jagla, A. & Mandelkow, E. Tubulin oligomers and microtubule oscillations. *Eur. J. Biochem.* **178,** 61–69 (1988).
22. Pojman, J. A. & Epstein, I. R. Convective effects on chemical waves. 1. Mechanisms and stability criteria. *J. Phys. Chem.* **94,** 4966–4972 (1990).
23. Epstein, I. R. & Pojman, J. A. *An Introduction to Nonlinear Chemical Dynamics: Oscillations, Waves, Patterns, and Chaos*. (Oxford University Press, 1998).
24. Nagypal, I., Bazsa, G. & Epstein, I. R. Gravity-induced anisotropies in chemical waves. *J. Am. Chem. Soc.* **108,** 3635–3640 (1986).
25. Tena-Solsona, M. *et al.* Non-equilibrium dissipative supramolecular materials with a tunable lifetime. *Nat. Commun.* **8,** 15895 (2017).
26. Maiti, S., Fortunati, I., Ferrante, C., Scrimin, P. & Prins, L. J. Dissipative self-assembly of vesicular nanoreactors. *Nat. Chem.* **8,** 725–731 (2016).
27. Mishra, A. *et al.* Biomimetic temporal self-assembly via fuel-driven controlled supramolecular polymerization. *Nat. Commun.* **9,** 1295 (2018).
28. Jalani, K., Dhiman, S., Jain, A. & J. George, S. Temporal switching of an amphiphilic self-assembly by a chemical fuel-driven conformational response. *Chem. Sci.* **8,** 6030–6036 (2017).

29. Boekhoven, J., Hendriksen, W. E., Koper, G. J. M., Eelkema, R. & Esch, J. H. van. Transient assembly of active materials fueled by a chemical reaction. *Science* **349,** 1075–1079 (2015).
30. Scott, S. K. *Chemical Chaos*. (Clarendon Press, 1993).
31. Hammele, M. & Zimmermann, W. Modeling oscillatory microtubule polymerization. *Phys. Rev. E* **67,** (2003).
32. Nicolis, G. & Prigogine, I. *Self-organization in nonequilibrium systems*. (Wiley, 1977).
33. Zhang, Y., Tsitkov, S. & Hess, H. Complex dynamics in a two-enzyme reaction network with substrate competition. *Nat. Catal.* **1,** 276–281 (2018).
34. Orlova, T. *et al.* Revolving supramolecular chiral structures powered by light in nanomotor-doped liquid crystals. *Nat. Nanotechnol.* **13,** 304–308 (2018).
35. Gelebart, A. H. *et al.* Making waves in a photoactive polymer film. *Nature* **546,** 632–636 (2017).
36. Sorrenti, A., Leira-Iglesias, J., Markvoort, A. J., de Greef, T. F. A. & Hermans, T. M. Non-equilibrium supramolecular polymerization. *Chem. Soc. Rev.* **46,** 5476–5490 (2017).
37. Sorrenti, A., Leira-Iglesias, J., Sato, A. & Hermans, T. M. Non-equilibrium steady states in supramolecular polymerization. *Nat. Commun.* **8,** 15899 (2017).

Acknowledgements

This work was financially supported by the Region Alsace, University of Strasbourg Institute for Advanced Study (USIAS), LabEx grant 'Suproscill' (CSC-THE-17), and ERC-2017-STG 'Life-Cycle' (757910). We acknowledge Thomas Ebbesen, Cyriaque Genet, and Marcus Seidel for help with the NIR static light scattering.

Author contributions

J.L.–I. and T.M.H. designed and performed the experiments, and analysed data. J.L.–I. performed the synthesis. A.T. performed static and dynamic light scattering experiments. A.T. and T.A. developed near-infra red static light scattering and interpreted the results. J.L.–I., A.T. and T.A. carried out the NIR static light scattering experiments. M.S. and T.M.H. performed modelling and interpretation of the results. J.L.–I. and T.M.H. wrote the paper. All authors discussed about the results, and commented on the manuscript. T.M.H. conceived the overall project and supervised the research.

Competing interests

The authors declare no competing interests.

Additional Information

Supplementary information is available in the online version of the paper.
Reprints and permission information is available online at www.nature.com/reprints.
Correspondence and requests for materials should be addressed to T.M.H.

Figure Captions

Fig. 1. Kinetics of redox fuelled PDI assembly and disassembly. a, **PDI** is reduced to $\mathbf{PDI}^{2-}$ upon addition of $Na_2S_2O_4$. Spontaneous oxidation in air leads first to radical anion $\mathbf{PDI}^{\bullet-}$ and then to neutral **PDI**. **b**, After one redox cycle (i.e., reduction to $\mathbf{PDI}^{2-}$ and oxidation to $\mathbf{PDI_{mon}}$, k_{red} and k_{ox}, respectively), $\mathbf{PDI_{mon}}$ grows via a cooperative polymerisation mechanism with nucleation k_{nuc}, elongation k_{el}, and fragmentation k_{frag} constants. The system is also characterized by a size-dependent reduction rate for $\mathbf{PDI_{assem}}$ ($k_{red,p}$, see data in panel d). **c**, The degree of polymerisation α as a function of time at different seeding per cent and **PDI** concentrations (see methods). Global fitting was used (solid lines) with a saturating elongation + fragmentation model[14,19] yielding: k_{nuc} = 0.069 ± 0.002 M^{-1} min^{-1}, k_{el} = 4.5•10^6 ± 4•10^5 M^{-1} min^{-1}, k_{frag} = 2.38•10^{-5} ± 2.8•10^{-6} min^{-1}, K_e = 1.80•10^{-5} ± 1.5•10^{-6} M, nucleus size n = 2 and error MRE = 0.0015. **d**, Reduction kinetics followed by stopped-flow where 80 μL of a 100 μM $\mathbf{PDI_{mon}}$ solution and 80 μL of a 50 mM $Na_2S_2O_4$ solution were loaded in syringes and quickly mixed at defined intervals. Over time $\mathbf{PDI_{mon}}$ grows to $\mathbf{PDI_{assem}}$ in the syringe, leading to slower kinetics shown in the insets. Two processes are observed: one exponential with time constant τ_1 and one sigmoidal with constant τ_2, which increase over time (see main text and methods). The red dashed line indicates the transition between the two processes. The reduction kinetics were followed at the characteristic dianion bands of $\mathbf{PDI}^{2-}$ at 612 nm.

Fig. 2. Supramolecular oscillations. a, Three different states (steady state **SS**, oscillations **OSC**, and precipitation **PR**) were observed in a semi-batch reactor under continuous influx of chemical fuel ($Na_2S_2O_4$).

b, The phase space of **PDI** concentration vs. flow rate of $Na_2S_2O_4$. **c**,**d**,**e**, The different states of a 100 μM **PDI** solution are shown (only the red channel intensity is shown for simplicity), **c**, a first steady state (**SS**) can be kept at low flow rates in which mostly neutral **PDI** is observed. **d**, oscillations (**OSC**) were observed by increasing the flow rate. **e**, higher flow rates lead to a state with mostly $\mathbf{PDI}^{2-}$ where precipitation (**PR**) occurs after ~40 min. **f**, CIE 1931 coordinates (x, y) coding for the red, green and blue channels. See the main text for a description of the indices i–v. **g,** Scattering intensity (left axis, black line) and red colour intensity (right axis, red line) of **PDI** (i, t = 20 min) vs time during two oscillations. The decrease of the scattering and red channel intensity indicates the formation of $\mathbf{PDI}^{\bullet-}$ and $\mathbf{PDI}^{2-}$ species (ii, t = 25 min, and v, t = 38 min) and a mostly disassembled state. Oxidation leading to $\mathbf{PDI}_{\mathbf{mon}}$ is apparent from the increase of the red channel intensities and pink color (iii, t = 34 min and vi, t = 42 min). Self-assembly of $\mathbf{PDI}_{\mathbf{mon}}$ into $\mathbf{PDI}_{\mathbf{assem}}$ leads to an increase in scattering intensity and visible turbidity in the solution (iv, t = 36.3 min, and vii, t = 48 min, and viii, t = 59 min). See Supplementary Video 1.

Fig. 3 Supramolecular oscillator model. a, The nucleation-elongation-fragmentation model is expanded with chemical fuels, i.e., reduction to $\mathbf{PDI}^{\bullet-}$ or $\mathbf{PDI}^{2-}$ species *R* and the oxidation back to $\mathbf{PDI}_{\mathbf{mon}}$ species (here *O*). **b**, Phase space plot as a function of the reduction and oxidation rates (k_{red} and k_{ox}, respectively) shows three different states: steady-state 'SS', oscillations 'OSC' and unphysical solutions 'US'. The top inset corresponds to the vertical cut through the oscillating window 'OSC' (along the solid line). The bottom inset shows the horizontal cut (along the dashed line). Initial conditions: $[P] = 1 \cdot 10^{-8}$ M, $[M] = 1 \cdot 10^{-7}$ M, $[R] = 5 \cdot 10^{-6}$ M, $[m]_{tot} = 1 \cdot 10^{-5}$ M; constants: $k_{frag} = 3 \cdot 10^{-4}$ s^{-1}, $k_{nuc} = 4 \cdot 10^{-4}$ M^{-1} s^{-1}, $k_{el} = 400$ M^{-1} s^{-1}. **c**, Reduced damping for smaller values of k_{frag} up to the point of nearly sustained oscillations (black line).

Fig. 4. Supramolecular traveling fronts and patterns. a, A rectangular 3D printed chip (50 x 25 mm) with two parallel glass slides spaced by 1 mm was used. A $\mathbf{PDI}_{\mathbf{mon}}$ solution was immediately injected into the chip. Then, $\mathbf{PDI}_{\mathbf{assem}}$ seeds (30 μL of a 1h old $\mathbf{PDI}_{\mathbf{mon}}$ solution) were added from one side of the chip. **b,** A traveling front in adjacent volumes was observed using a colour CCD equipped stereoscope (cf. Supplementary Video 2). The brightness/contrast has been increased to better show the front. **c**, The kymograph shows the progressive decrease in velocity of the front (extracted from Supplementary Video 2). **d**, The top glass cover slide was replaced by mineral oil permitting diffusion of O_2 and near-frictionless fluid transport. A $\mathbf{PDI}^{2-}$ solution (100 μM) was poured into the chip and covered by oil. An outward moving front (dashed area) was observed showing oxidation to $\mathbf{PDI}_{\mathbf{mon}}$. Simultaneously, a single massive convection cell is formed leading to an alignment of $\mathbf{PDI}_{\mathbf{assem}}$ structures in the direction of the flow (see Supplementary Video 5). **e**, Transient formation of polygons (appearing after ~ 30 min) was observed while performing propagating front experiments with identical conditions to those as shown in panel **a**.

Methods

PDI system. PDI was synthesized according to our protocol described recently.[13] In short, **PDI** was prepared by imidization of perylene-3,4,9,10-tetracarboxylic acid dianhydride with ethylenediamine. Afterwards, amide coupling between the perylene diimide derivative and oligoethyleneglycol derived from gallic acid was performed yielding the target compound **PDI**.

Preparation of $\mathbf{PDI}_{\mathbf{mon}}$. A 100 μM **PDI** mother solution was prepared by dissolving **PDI** (1 mg, 0.60 μmol) in 50 mM borate buffer, pH 8. **PDI** solution (2 mL) was reduced to mostly monomeric $\mathbf{PDI}^{2-}$ by adding 2 μL of a 400 mM $Na_2S_2O_4$ solution (in borate buffer) under constant stirring (i.e., 1000 rpm). Spontaneous oxidation in air (O_2) leads to $\mathbf{PDI}^{\bullet-}$ and then to $\mathbf{PDI}_{\mathbf{mon}}$. Afterwards, $\mathbf{PDI}_{\mathbf{mon}}$ grows via a cooperative polymerisation mechanism yielding colloidal $\mathbf{PDI}_{\mathbf{assem}}$.

Dynamic light scattering (DLS). The intensity autocorrelation functions $g^{(2)}(q,\tau) \equiv \langle I(q,0)I(q,\tau)\rangle / \langle I(q,0)^2\rangle$ were measured on a home-built light scattering setup with an ALV7002 digital correlator using a laser diode at λ = 639 nm at a wavevector q = 0.0185 nm^{-1} (90° scattering angle). Measurements were performed on 100 μM **PDI**, $\mathbf{PDI}^{\bullet-}$ and $\mathbf{PDI}^{2-}$ every 60 s for 10 min. The relaxation dynamics were analysed by the inverse Laplace transformation $g^{(1)}(\tau) = \int_0^\infty H(\Gamma) e^{-\Gamma t} d\Gamma$ where $g^{(1)} = \sqrt{g^{(2)} - 1}$. Hydrodynamic radii R_H were then calculated using the Stokes-Einstein relation $R_H = k_B T/(6\pi\eta D)$ where $D = 1/(\tau q^2)$ and the root mean-squared deviation from the mean size of each state where determined fitting the hydrodynamic radius distribution with a Schultz distribution function. In order to perform the cooperative growth analysis of $\mathbf{PDI}_{\mathbf{mon}}$ (cf. Supplementary Figure 3), the intensity autocorrelation functions were fitted with a monoexponential decay function $g_1(t) = e^{-\Gamma t}$.

Kinetics of the cooperative polymerisation. A 100 μM **PDI** mother solution was prepared by dissolving **PDI** (1 mg, 0.60 μmol) in 50 mM borate buffer, pH 8. The different concentrations (i.e., 75, 50 and 25 μM) were prepared by diluting the mother solution with the corresponding amount of borate buffer solution in order to yield the desired concentration. Afterwards, 2 mL of each **PDI** solution was reduced by adding 2 μL of a 400 mM $Na_2S_2O_4$ solution (in borate buffer) at constant stirring rate (i.e., 1000 rpm). Spontaneous oxidation in air leads to $\mathbf{PDI}_{\mathbf{mon}}$ species. A 100 μM freshly oxidized $\mathbf{PDI}_{\mathbf{mon}}$ solution (1 mL) was aged for 1 h

in order to prepare **PDI$_{assem}$** seeds. Seeding experiments were performed by adding different amounts of seeds (i.e., 15, 10 and 5 % in v/v) to a 100 μM **PDI$_{mon}$** solution (final volume of the solution was 2 mL). Stirring experiments were performed on a 100 μM **PDI$_{mon}$** solution (2 mL) at different stirring rates (i.e., 1000, 750 and 500 rpm). Kinetics experiments were performed on a JASCO V-670 spectrophotometer equipped with a Peltier system as a temperature controller. Spectra (i.e., from 400 to 700 nm) were recorded in a 1 cm quartz cuvette at 25 ºC.

Reduction kinetics. The reduction kinetics of **PDI** to **PDI^{2-}** was monitored by stopped-flow (SFM-3, Bio-Logic). The OD intensity was followed at 612 nm (i.e., characteristic band of **PDI^{2-}**). A 100 μM solution was prepared by dissolving **PDI** (1 mg, 0.60 μmol) in 50 mM borate buffer, pH 8. Afterwards, 9 mL of a 100 μM **PDI** solution were reduced with 15 μL of a 400 mM $Na_2S_2O_4$ solution (in borate buffer) under constant stirring rate (1000 rpm). Immediately after oxidation, the freshly oxidized **PDI$_{mon}$** solution and 9 mL of a 40 mM $Na_2S_2O_4$ solution were added into the syringes. Then, 80 μL of freshly oxidized **PDI$_{mon}$** solution and 80 μL of $Na_2S_2O_4$ solution were quickly mixed. The reduction kinetics was followed for 90 min by doing data intervals of one minute. The data recording frequency was 0.2 ms for the first 2 s and 10 ms for one minute. The evolution of the time constant τ_1 was obtained from fitting the next expression $I = A \cdot \exp(\tau_1/t)$. The evolution of time constant τ_2 was obtained from fitting the next expression $y = A_2+(A_1-A_2)/(1 + \exp((t-t_0)/\tau_2))$. *A* values are constants.

Supramolecular oscillations. Oscillations were tracked with a Basler CCD camera and a diode-array spectrophotometer (Analytikjena, Specord S600). **PDI$_{mon}$** (2.25 mL) solutions (i.e., 100, 75, 50 and 25 μM) were measured under continuous influx of a 400 mM $Na_2S_2O_4$ solution at constant stirring rate (i.e., 1000 rpm) in a well-ventilated box (constant oxygen supply and light) for 12 hours. Different flow rates (from 0.45 to 0.9 μL/min) were studied in order to map the state space. Red, green and blue channels were recorded at 10 frames per second using a home-built matlab interface. UV-Vis spectra were recorded from 400 to 900 nm in 2 seconds, spectra were taken every 10 seconds. Waste and buffer experiment were performed by adding 250 μL of waste or buffer after defined times.

Near-IR light scattering experiments. The scattering intensity measurements during oscillations were performed by using a home-built setup (cf. Supplementary Figure 9). A 905 nm laser line was obtained from a CW tunable Ti:Sapphire laser (Spectra-Physics, Model 3900S) pumped by a Millennia eV (Spectra-Physics, 15W diode-pumped solid state laser). This wavelength was selected because none of the three species (**PDI**, **PDI$^{\bullet-}$** and **PDI^{2-}**) have absorption at 905 nm. The laser power was adjusted to be 300 mW. A collimated laser beam (d = 6 mm) was irradiated through the sample solution that was placed on a magnetic stirring plate. Scattered light was collected by a first lens (Thorlabs, f = 100 mm Plano-Convex lens) and focused by a second lens (Thorlabs, f = 25 mm Plano-Convex lens) on the InGaAs photodiode detector (Thorlabs, DET10N/M). The voltage output was recorded by a multichannel data logger (Pico Technology, ADC-20). Scattered light was collected from an off-centered position to avoid the disturbance by a vortex generated by a stirring bar inside solution.

Confocal measurements. Confocal micrographs were taken by using Zeiss LSM 710 confocal microscope system with 10 x magnification. The samples were excited by continuous-wave laser at 488 nm. The emission was measured from 500 nm to 700 nm using a spectral detector. Measurements were performed by taking 10 μL aliquots during oscillations. Measurements were performed on a 75 μM **PDI** solution.

Supramolecular traveling fronts. 1.5 mL of a 100 μM **PDI$_{mon}$** solution was injected into a 3D printed chip (50 x 25 mm). The chip was printed in VeroClear on a Stratasys Objet 30 printer and contains two glass cover slips separated by 1 mm. Solutions can be injected from either side of the chip. In order to perform the experiment, 30 μL of **PDI$_{assem}$** seeds or buffer (a freshly oxidized 100 μM **PDI$_{mon}$** solution aged for 1 hour) were injected on one side of the chip. Images were acquired using a stereoscope (Nikon SMZ7457) equipped with a CCD camera, frames were recorded every 10 seconds for ~1.5 hours, or using a ZEISS LSM 710 confocal microscope, frames were recorded every 1 second for 30 min.

Density measurements. The density of **PDI^{2-}**, **PDI$_{mon}$** and **PDI$_{assem}$** species was measured by using an Anton Paar DMA 500 density meter. 6 mL of a 100 μM **PDI** borate buffer solution was reduced to **PDI^{2-}** by adding 4 μL of a 400 mM $Na_2S_2O_4$ solution. The density of **PDI^{2-}** species was measured (2 mL / measurement was used). The density was measured after oxidation back to **PDI$_{mon}$** species and when **PDI$_{mon}$** was aged for 1h leading to **PDI$_{assem}$**. All measurements were repeated at least 4 times.

Oscillations, traveling fronts and patterns in a supramolecular system

Jorge Leira-Iglesias[1], Alessandra Tassoni[1], Takuji Adachi[1], Michael Stich[2] and Thomas M. Hermans[1]*

[1] University of Strasbourg, CNRS, ISIS UMR 7006, F-67000 Strasbourg, France. [2] Non-linearity and Complexity Research Group, Systems Analytics Research Institute, Engineering and Applied Science, Aston Triangle, Birmingham B4 7ET, United Kingdom. * e-mail: hermans@unistra.fr

Supplementary Information

Oscillations, traveling fronts and patterns in a supramolecular system

Jorge Leira-Iglesias[1], Alessandra Tassoni[1], Takuji Adachi[1], Michael Stich[2] and Thomas M. Hermans[1]*

Corresponding author: * hermans@unistra.fr

Contents:

Supplementary Section 1. UV-Vis and light scattering experiments

UV-Vis experiments showing the growth of **PDI$_{mon}$** to **PDI$_{assem}$** (i.e., black to red spectra in Supplementary Fig. 1).[1] A new band appears at 528 nm having a sigmoidal time progression indicating that **PDI** assembles via a cooperative polymerization mechanism (see section 2 below for a more detailed analysis). UV-Vis spectra are shown as optical density *OD* since there is contribution of scattering as well as absorption. We assume that the optical density is directly proportional to the degree of aggregation α and is experimentally determined as: $[OD]_{528nm} = \alpha[OD]_{PDI_{assem,528nm}} + (1-\alpha)[OD]_{PDI_{mon,528nm}}$.[2] Neutral **PDI$_{assem}$** structures are ~2 μm in size, whereas reduced **PDI$^{\bullet-}$** and **PDI^{2-}** are only ~100 nm at 100 μM (Supplementary Fig. 2). Dynamic and static light scattering show the size and scattering progression of the **PDI$_{mon}$** cooperative growth (Supplementary Fig. 3).

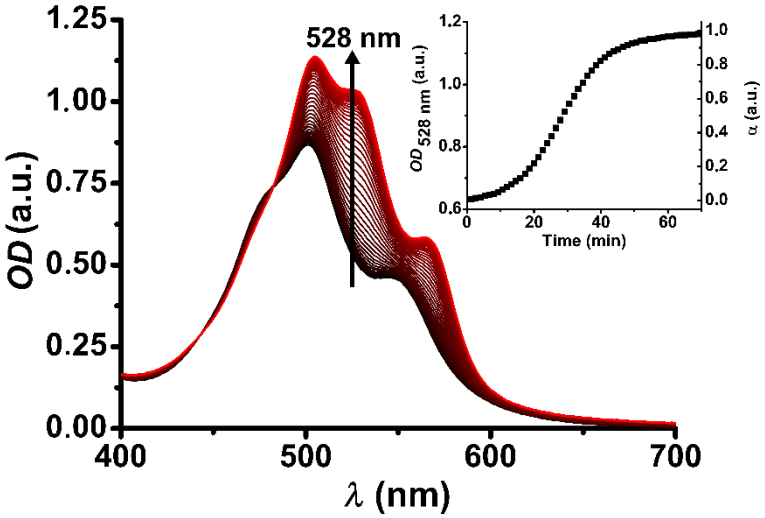

Supplementary Figure 1. UV-Vis spectroscopy. UV-Vis spectra of a 100 μM **PDI$_{mon}$** borate buffer solution (**PDI** solution was reduced to **PDI^{2-}** and spontaneously oxidized back to neutral **PDI**, see Methods) at 500 rpm. The inset shows the time progression of the 528 nm band which can be used to track the cooperative polymerization.

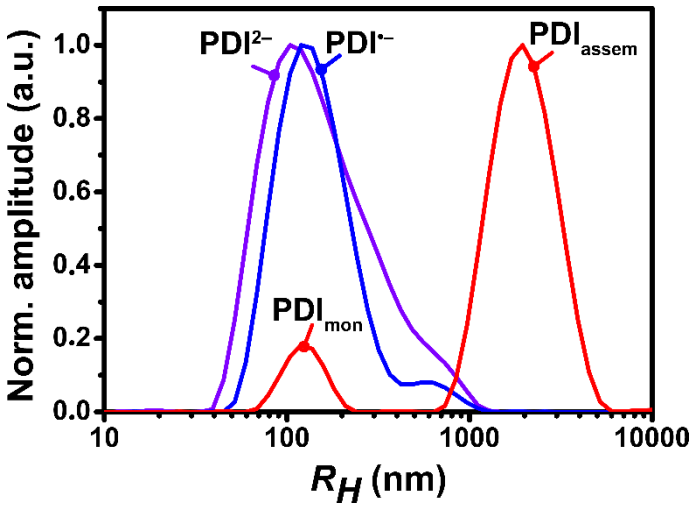

Supplementary Figure 2. Dynamic (visible, 639 nm) light scattering measurements. Size distributions are shown for **PDI** (red curve), **PDI$^{\bullet-}$** (blue curve), and **PDI^{2-}** (purple curve) at 100 μM in borate buffer solution.

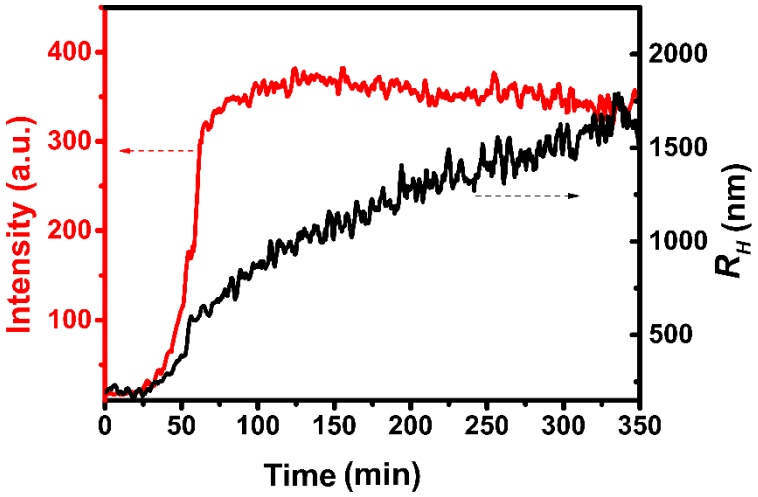

Supplementary Figure 3. Static and dynamic (visible, 639 nm) light scattering during the progression of PDI^{2-} to PDI_{mon} to PDI_{assem}. Hydrodynamic radius (black, right axis) from dynamic light scattering, and static light scattering intensity (red, left axis) vs time of supramolecular polymerization at 100 μM (non-stirred, since we cannot do DLS while stirring). The evolution of the size vs time has a sigmoidal time progression in agreement with observations by UV-Vis spectroscopy (cf. Supplementary Figure 1). **PDI^{2-}** absorbs at 639 nm, which decreases the total scattered intensity. When **PDI^{2-}** disappears due to oxidation, a large jump in static light scattering intensity can be seen (t ~ 50 min). Therefore, visible static light scattering cannot be used quantitatively. The intensity autocorrelation functions for dynamic light scattering were fitted with a monoexponential decay function $g_1(t) = e^{-\Gamma t}$.

Supplementary Section 2. Cooperative polymerization mechanism

PDI$_{mon}$ assembles via a cooperative polymerization mechanism into **PDI$_{assem}$** structures.[1] We determined the half times (i.e., the time needed for half of the **PDI** molecules to be assembled) at different concentrations and used them to discriminate between various available models.[3] A scaling factor γ can be obtained from the plot of the half times vs. concentration (Supplementary Fig. 4). The scaling factor γ is 0.485 ± 0.036 which indicates that **PDI** polymerization involves more processes than simple nucleation and elongation steps. In addition, the value of γ suggests that fragmentation is also involved in the polymerization mechanism.[3] The data were analysed using three different analytical models (using the AmyloFit platform)[3]: nucleation-elongation, nucleation-elongation including fragmentation, and saturating elongation + fragmentation (see Supplementary Fig. 5 and Fig. 1c in the main text). The fitting improves when the fragmentation step is included into the model judged from the mean residual error (MRE), when compared to simple nucleation-elongation. The saturating elongation and fragmentation model gives the best fitting (i.e., lowest mean residual error, Supplementary Fig. 6) which indicates that the elongation involves multiple steps and thus, **PDI** polymerization is more complex than simple nucleation-elongation. In addition, nucleus size 2 gives the best fitting for all models (Supplementary Fig. 6).

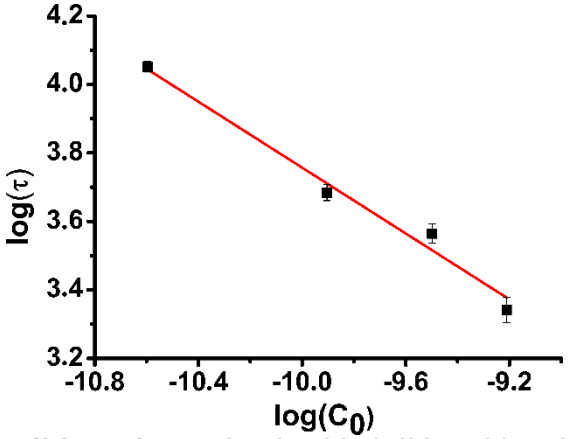

Supplementary Figure 4. Half times plot. Log-log plot of the half time of the polymerization at different **PDI** concentrations (i.e., 100, 75, 50 and 25 μM). The scaling exponent γ was obtained by fitting the following equation: $\log(\tau) = \gamma \cdot \log(C_0) + k$. The slope yields the scaling exponent γ = -0.485 ± 0.036.

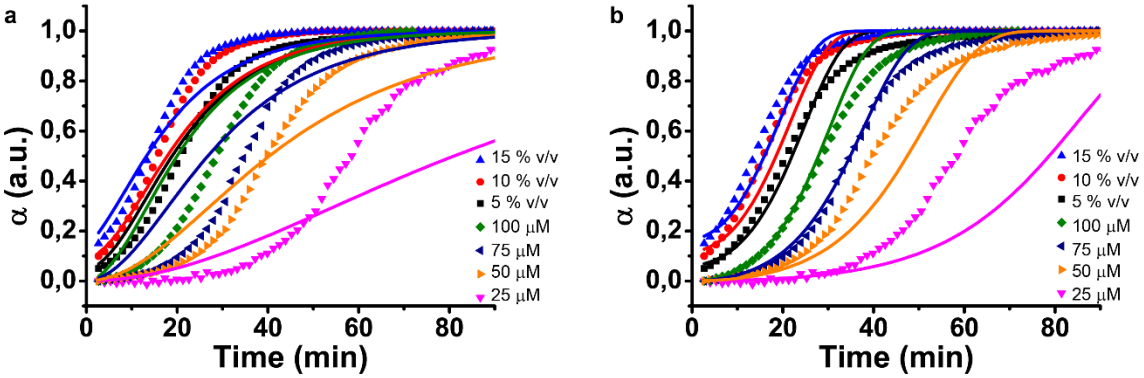

Supplementary Figure 5. Alternative model fits of PDI supramolecular polymerization. PDI supramolecular polymerization of the different **PDI** concentrations at 1000 rpm (degree of aggregation α indicates the growth of **PDI** assemblies). Seeding experiments (15, 10 and 5 % in v/v of 1 h **PDI$_{mon}$** aged solution, i.e., seeds were added to a freshly oxidized **PDI$_{mon}$** solution) were performed on 100 μM **PDI$_{mon}$** borate buffer solution at the same stirring rate (i.e., 1000 rpm). Afterwards, the data was analysed with **a,** a simple nucleation-elongation model that gives k_{nuc} =2.6 $M^{-1} \cdot min^{-1}$, k_{el} = 1.1•10^5 $M^{-1} \cdot min^{-1}$, k_{rel} = 3.6•10^{-13} min^{-1}, n = 2 and mean residual error (MRE) = 0.016. **b,** a nucleation-elongation model that includes fragmentation that gives k_{nuc} =26 $M^{-1} \cdot min^{-1}$, k_{el} = 1.8•10^3 $M^{-1} \cdot min^{-1}$, k_{rel}= 1•10^{-15} min^{-1}, k_{frag} = 0.048 min^{-1}, n = 2 and MRE = 0.0058.

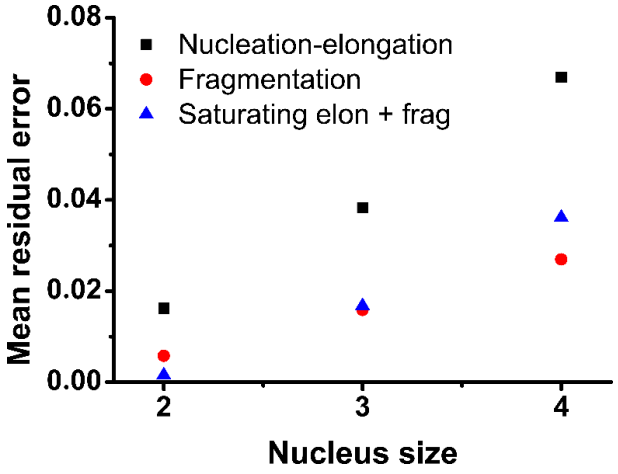

Supplementary Figure 6. Effect of the nucleus size on the error of fitting the polymerization mechanism. Mean residual error of the global fitting of the nucleation-elongation (black squares), nucleation-elongation including fragmentation (red dots) and saturating elongation + fragmentation models (blue triangles) vs nucleus size.

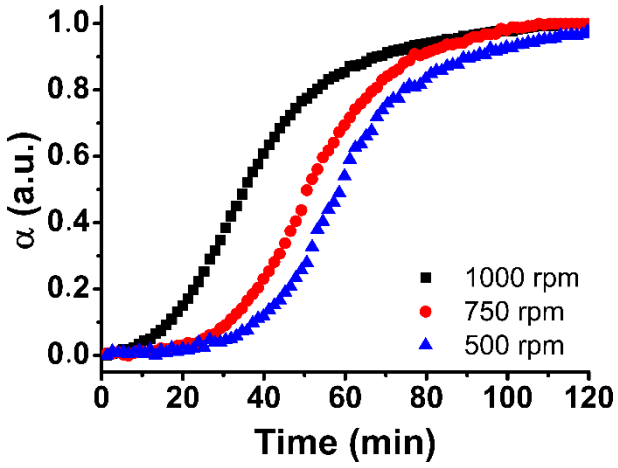

Supplementary Figure 7. Cooperative polymerization of PDI at different stirring rates. 2 mL of a 100 μM **PDI** borate buffer solution was reduced to **PDI**$^{2-}$ upon addition of 2 μL of 400 mM $Na_2S_2O_4$ solution. After spontaneous oxidation in air, the cooperative growth of **PDI**$_{mon}$ was followed at different stirring rates (1000, 750 and 500 rpm).

Supplementary Section 3. One redox cycle

A colour CCD camera permits to track separately red, blue and green colour channels of a **PDI** solution. Combined with a fast diode-array spectrophotometer, it can be used to determine the relative concentration of the different species present in solution. Prior to reducing the system, the starting values of red and blue channel and the diode-array (i.e., black line in the inset, Supplementary Fig.8) confirm the presence of as prepared **PDI** assemblies. The intensity of the red channel drops quickly (i.e., intensity goes from ~80 to ~40) upon addition of reductant $Na_2S_2O_4$. The diode-array (i.e., purple dash-dot line in the inset, Supplementary Figure 8) confirms the formation of $\mathbf{PDI^{2-}}$. $\mathbf{PDI_{mon}}$ is reached after spontaneous oxidation in the air. The blue channel intensity increases and the red channel decreases indicating the transient formation of $\mathbf{PDI^{\bullet-}}$ (the spectrum shows the characteristic bands of $\mathbf{PDI^{\bullet-}}$ at 727 and 813 nm, blue dashed spectrum in the inset of Supplementary Fig. 8). Afterwards, the red channel intensity quickly increases and the blue channel intensity decreases showing the presence of $\mathbf{PDI_{mon}}$ (pink dotted spectrum in the inset). In addition, a slow sigmoidal increase in both channels indicates the cooperative growth of $\mathbf{PDI_{mon}}$ to $\mathbf{PDI_{assem}}$. Diode-array measurements (performed simultaneously) confirmed the presence of $\mathbf{PDI_{assem}}$ (green dotted spectrum in the inset). In short, the colour camera and diode-array UV-Vis detector permit to track all the species present in a full redox cycle **PDI** → $\mathbf{PDI^{2-}}$ → $\mathbf{PDI^{\bullet-}}$ → $\mathbf{PDI_{mon}}$ → $\mathbf{PDI_{assem}}$.

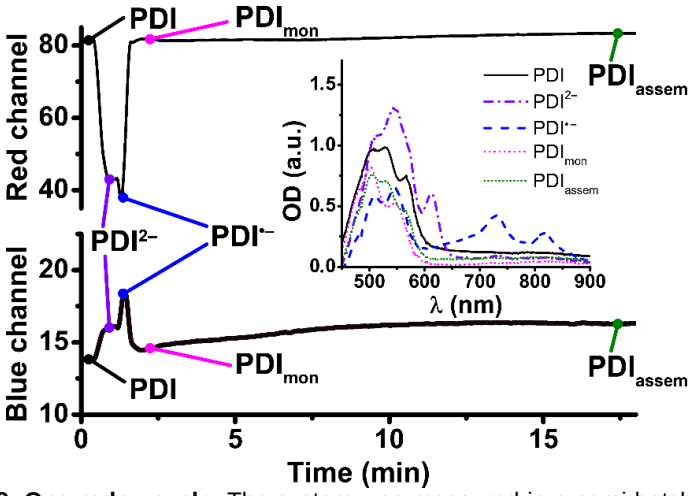

Supplementary Figure 8. One redox cycle. The system was measured in a semi-batch reactor at 1000 rpm with a CCD camera and diode-array UV-Vis detector. 2.25 mL of a 25 μM **PDI** borate buffer solution is reduced to $\mathbf{PDI^{2-}}$ upon the addition of 2 μL of 400 mM $Na_2S_2O_4$ solution. Afterwards, $\mathbf{PDI^{2-}}$ was oxidized back to $\mathbf{PDI_{mon}}$ via $\mathbf{PDI^{\bullet-}}$ formation. $\mathbf{PDI_{mon}}$ grows via a cooperative polymerization mechanism leading to $\mathbf{PDI_{assem}}$. The inset shows the spectra of all different species present in solution along 1 redox cycle (i.e. **PDI** → $\mathbf{PDI^{2-}}$ → $\mathbf{PDI^{\bullet-}}$ → $\mathbf{PDI_{mon}}$ → $\mathbf{PDI_{assem}}$).

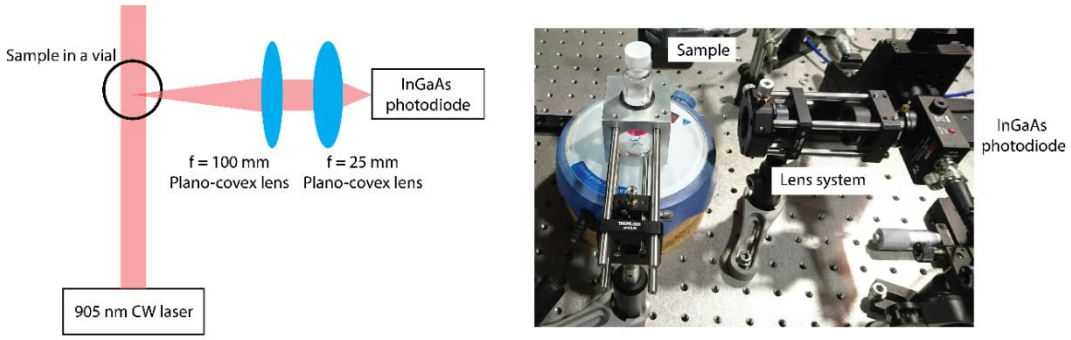

Supplementary Figure 9. Scheme of the near-infra red light scattering setup using a 905 nm laser. The scattering intensity was recorded using a home-built setup (photo shown on the right). This wavelength was selected because none of the three species (**PDI**, $\mathbf{PDI^{\bullet-}}$ or $\mathbf{PDI^{2-}}$) have light absorption at 905 nm (cf. Supplementary Figure 8).

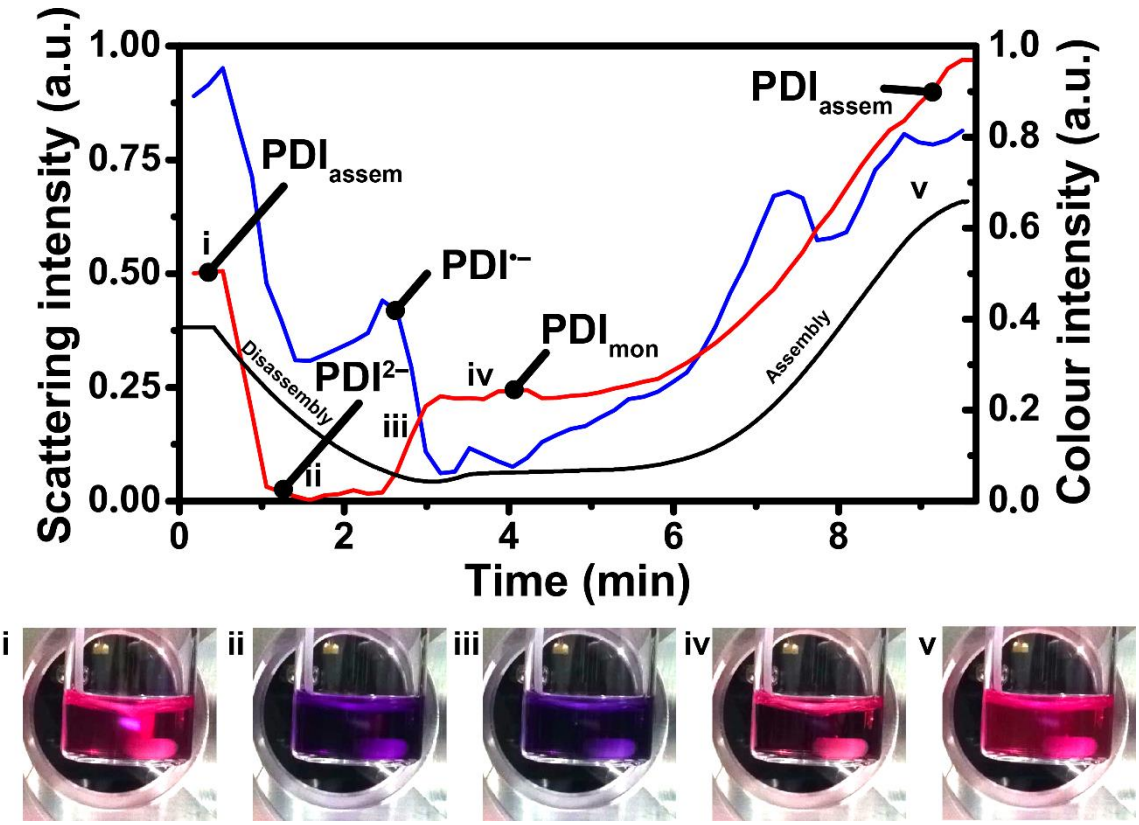

Supplementary Figure 10. Near-infra red light scattering intensity and colour tracking of PDI species during one redox cycle. The system was measured in a semi-batch reactor at 1000 rpm using a 905 nm laser (cf. Supplementary Figure 9) and a camera. **PDI** (i at t = 0 min, 2.25 mL of a 25 μM solution) is reduced to **PDI^{2-}** upon the addition of the reductant (ii, t = 1.2 min) inducing a decrease in the scattering intensity (black curve, left axis) and in the red and blue channel intensity (red and blue curves on the right axis, respectively). Afterwards, **PDI^{2-}** was oxidized back to **PDI$_{mon}$** (iv, t = 4 min) via **PDI$^{\bullet-}$** formation (iii, t = 2.75 min), while reaching a minimum in the scattering intensity and a maximum in the blue channel. **PDI$_{mon}$** grows via a cooperative polymerization mechanism leading to **PDI$_{assem}$** (v, t = 9 min) where an increase of the scattering intensity and the red/blue channel can be observed.

Supplementary Section 4. Supramolecular oscillator

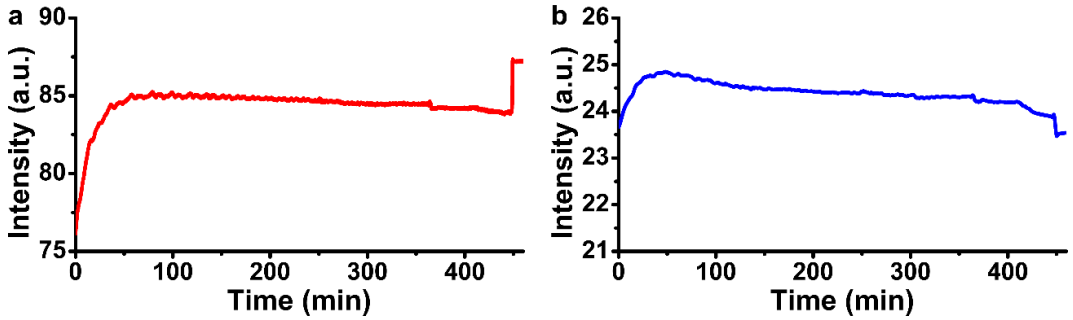

Supplementary Figure 11. Steady state 'SS'. 2.25 mL of a 100 μM **PDI** borate buffer solution was reduced to $\mathbf{PDI^{2-}}$ by adding 2 μL of a 400 mM $Na_2S_2O_4$ solution. Constant inflow of reductant (0.7 μL/min) was set once $\mathbf{PDI_{mon}}$ was present in solution. After 450 min, inflow of chemical fuel was stopped leading to **a,** a minor increase of the intensity of the red channel, **b,** a minor decrease of the intensity of the blue channel and thus, full oxidation to $\mathbf{PDI_{assem}}$.

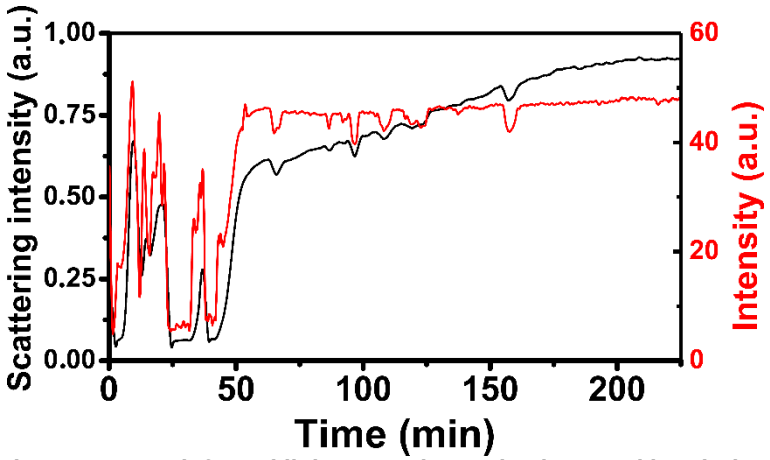

Supplementary Figure 12. Near-infra red light scattering and colour tracking during supramolecular oscillations. The scattering intensity (left axis, black line) and the red channel colour intensity (right axis, red line) of a 75 μM **PDI** solution are tracked during oscillations in a semi-batch reactor at 1000 rpm using a 905 nm laser line and a camera (see methods).

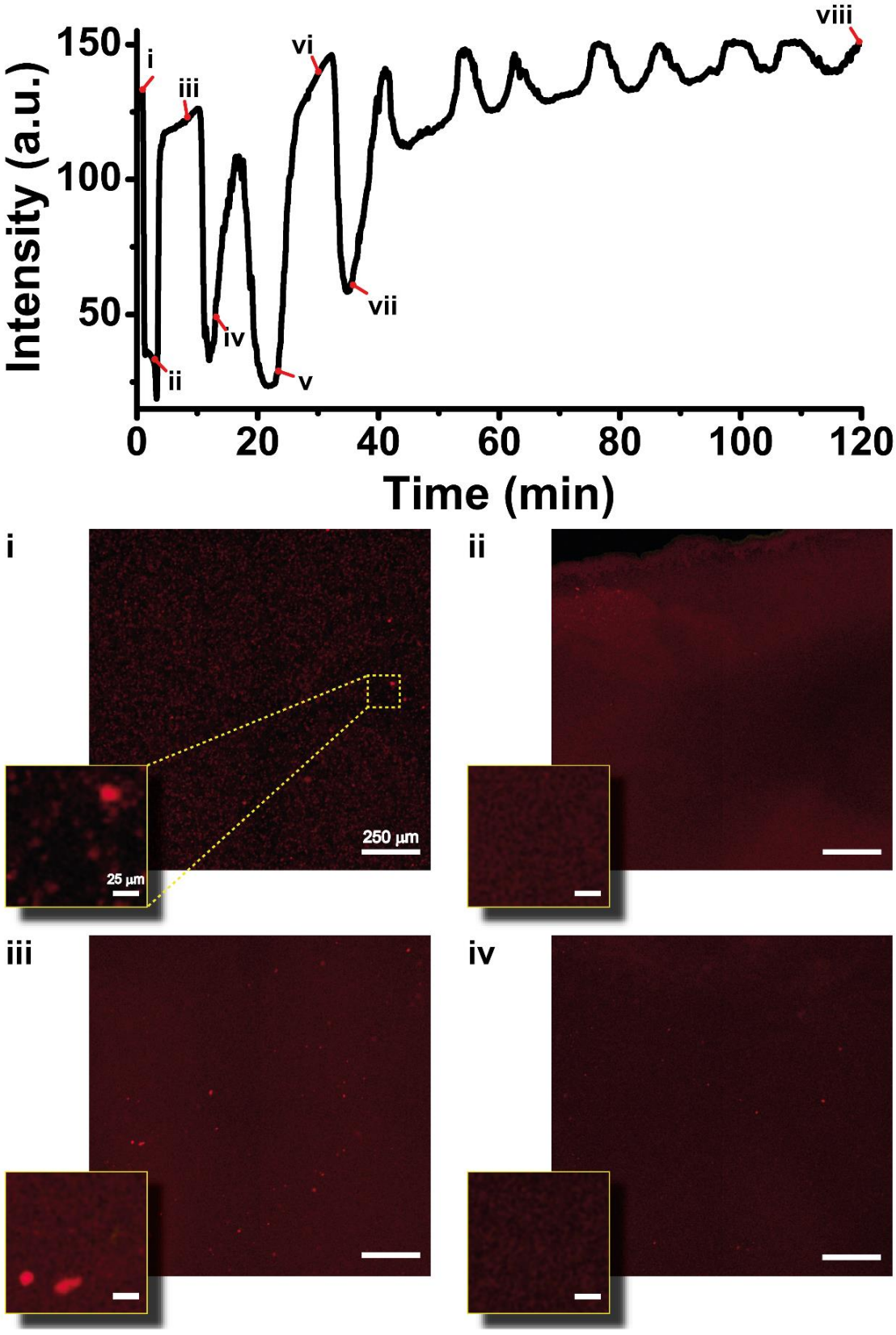
Intensity (a.u.)
150
100
50
0
20
40
60
80
100
120
Time (min)
i
ii
iii
iv
v
vi
vii
viii
250 µm
25 µm

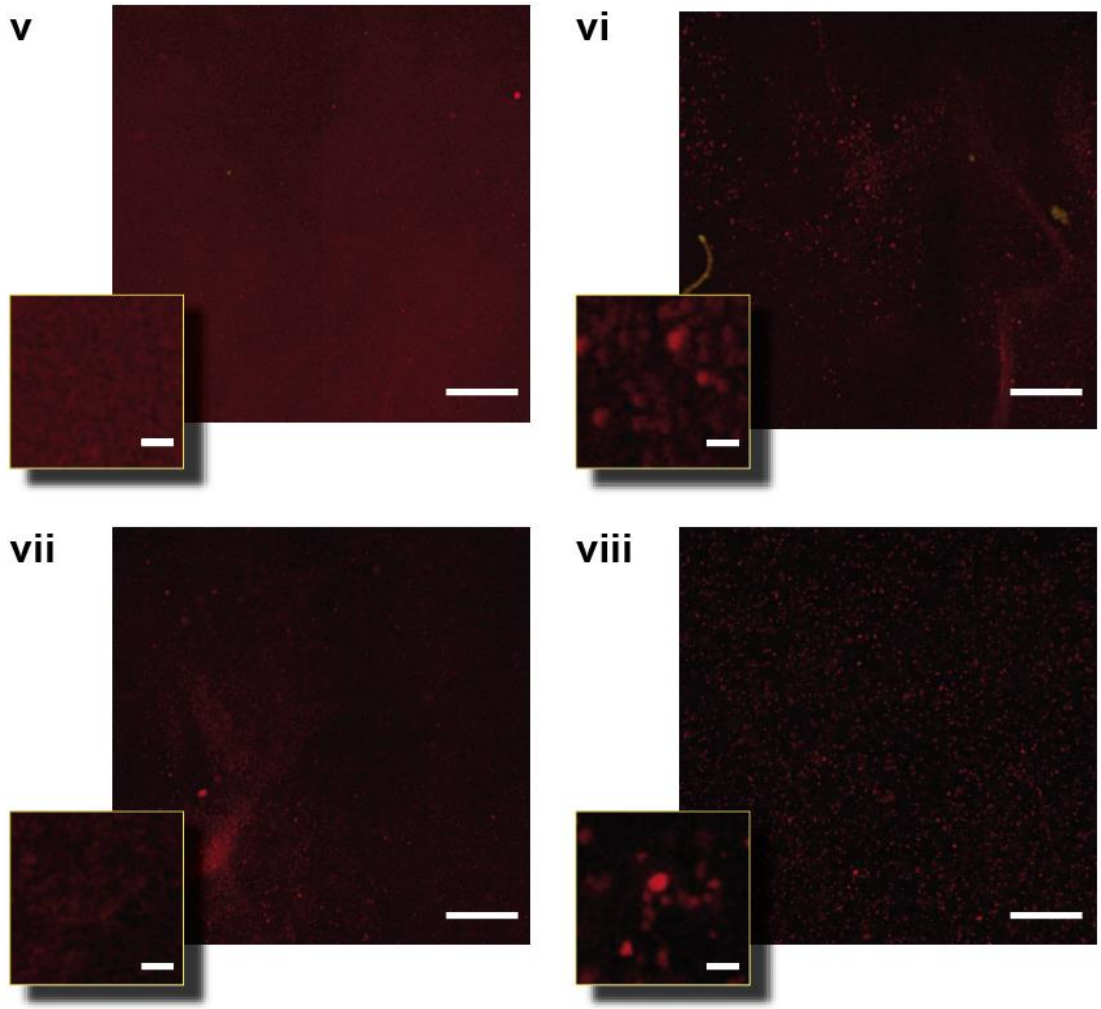

Supplementary Figure 13. Confocal micrographs during supramolecular oscillations. Aliquots from a 75 μM **PDI** solution during oscillations (followed with a CCD colour camera, black line shows red channel intensity) were measured using a Zeiss LSM 710 confocal microscopy (see methods). Red emissive assemblies can be observed in a freshly prepared **PDI** solution (i, *t* = 0 min). **PDI^{2-}** is formed after addition of $Na_2S_2O_4$ inducing complete disassembly at the resolution of the microscope (ii, *t* = 2 min). Oxidation leads to **PDI$_{mon}$** which grows via cooperative polymerization. Red emissive assemblies can be observed when **PDI$_{assem}$** are present in solution (iii, *t* = 10 min). The assemblies mostly disappear during oscillations (iv, *t* = 13 min, v, *t* = 23.3 min, and vii, *t* = 35.6 min). Micrograph viii (t = 120 min) shows that the number of **PDI$_{assem}$** stays consistently high in the damped region (after t ~60 min). In general, only during the first 3-5 large scale oscillations do all of the **PDI$_{assem}$** disappear.

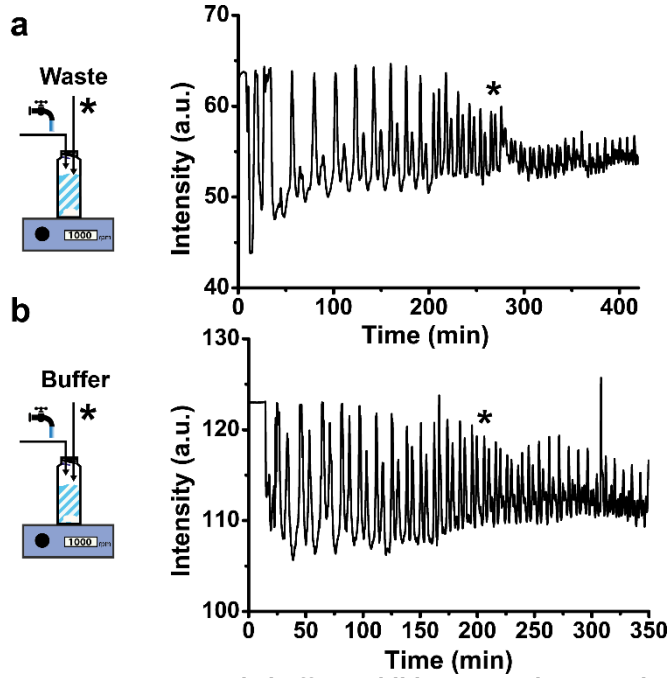

Supplementary Figure 14. Waste and buffer addition experiments during supramolecular oscillations. 2.25 mL of a 100 μM **PDI** borate buffer solution was reduced to **PDI^{2-}** by adding 2 μL of a 400 mM $Na_2S_2O_4$ solution. Constant inflow of reductant (0.7 μL/min) was set once **PDI$_{mon}$** was in solution. **a,** 250 μL of a 400 mM old dithionate solution (prepared the day before) was added after 250min, **b,** 250 μL of buffer solution was added after 225 min. These experiments show that neither waste accumulation nor volume changes significantly change the oscillations.

Supplementary Section 5. Supramolecular oscillator model

The model can be derived using basic nucleation-elongation-fragmentation kinetics.[4] Continuation analysis and simulations of the model were performed with MatCont (downloadable from https://sourceforge.net/projects/matcont/). Simulations were done with the ODE45 routine provided by MatCont 5.1 within Matlab 8.4.0. The master equation for an ensemble of polymers is given by the time evolution of the concentrations $f\,(t,j)$, where j indicates the length of the polymer and where we suppress the time dependence in the notation in the following:

$$\frac{\partial f(j)}{\partial t} = 2mk_{el}f(j-1) - 2mk_{el}f(j) + 2k_{red}f(j-1) - 2k_{red}f(j) - f_{frag}(j-1)f(j) + 2k_{frag}\sum_{i=j+1}^{\infty} f(i) + k_{nuc}m^{n_c}\delta_{j,n_c} \quad (1)$$

Depolymerisation is assumed to occur only in the reduction step to the *R* type of monomers (vs monomers that are oxidised *O*, which can polymerize). No fusion (inverse of fragmentation) or secondary nucleation is considered here. The condition $f(j) = 0$ for all $j < n_c$, where $n_c \geq 2$ is the critical nucleus size for the filament growth. From Eq. (1) we derive the kinetic equations for the number *P* and mass concentrations *M*:

$$P(t) = \sum_j f(t,j) \text{ and } M(t) = \sum_j j \cdot f(t,j) \quad (2)$$

By taking the sum over j on both sides of Eq. (1). We obtain

$$\frac{d[P]}{dt} = k_{frag}([M] - (2n_c - 1)[P]) + k_{nuc}[O]^{n_c} \quad (3)$$

$$\frac{d[M]}{dt} = 2(k_{el}[O] - k_{red} - k_{frag}n_c(n_c - 1)/2)[P] + n_c k_{nuc}[O]^{n_c} \quad (4)$$

where the contribution $k_{red}f(n_c)$ has been neglected to obtain a closed expression. The contribution of the dissociation of the nucleus to the overall dynamics is assumed to be small. The mathematical structure of the kinetic equations depends on the value of the critical nucleus size

n_c. For simplicity, we fix $n_c = 2$ for the remainder of this article (simulations not displayed here show that oscillations can also be found for n_c = 3,4) and we obtain:

$$\frac{d[P]}{dt} = -3k_{frag}[P] + k_{frag}[M] + k_{nuc}[O]^2 \quad (5)$$

$$\frac{d[M]}{dt} = -2(k_{frag} + k_{red})[P] + 2k_{el}[P][O] + 2k_{nuc}[O]^2 \quad (6)$$

The reduced type of monomers *R* obeys the following mass-action expression

$$\frac{d[R]}{dt} = k_{red}[P] - k_{ox}[R] \quad (7)$$

and the overall mass conservation yields for the concentration of oxidized monomers *O* (with $[m]_{tot}$ being the total mass):

$$[O] = [m]_{tot} - [M] - [R] \quad (8)$$

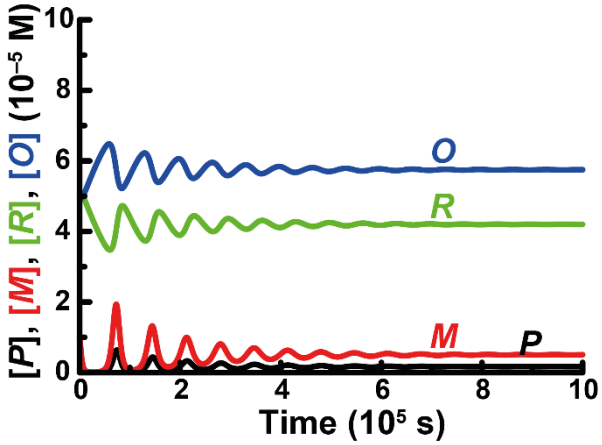

Supplementary Figure 15. Numerical simulations of oscillations in all species. All variables (*P*, *M*, *R* and *O*) show oscillating behaviour. Initial conditions: $[P] = 1 \cdot 10^{-8}$ M, $[M] = 1 \cdot 10^{-7}$ M, $[R] = 5 \cdot 10^{-6}$ M, $[m]_{tot} = 1 \cdot 10^{-5}$ M; constants: $k_{nuc} = 4 \cdot 10^{-4}$ M^{-1} s^{-1}, $k_{el} = 400$ M^{-1} s^{-1}, $k_{frag} = 3 \cdot 10^{-4}$ s^{-1}, $k_{red} = 1.5 \cdot 10^{-3}$ s^{-1}, $k_{ox} = 5 \cdot 10^{-6}$ s^{-1}.

Supplementary Section 6. Supramolecular fronts and patterns

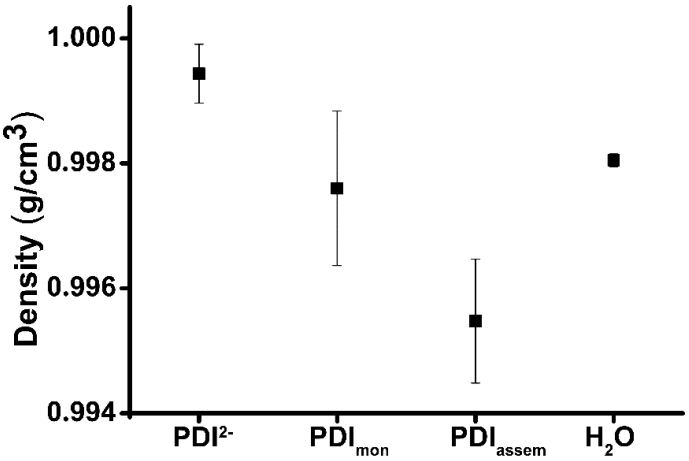

Supplementary Figure 16. Density measurements. 6 mL of a 100 μM **PDI** borate buffer solution was reduced to **PDI^{2-}** by adding 4 μL of a 400 mM $Na_2S_2O_4$ solution. The density of **PDI^{2-}** was measured. Afterwards, the density of **PDI$_{mon}$** was measured just after oxidation (in air) to the neutral state. **PDI$_{mon}$** was aged for 1h leading to **PDI$_{assem}$**. Water was measured as a control experiment. All measurements were repeated at least 4 times. The difference in density between **PDI$_{mon}$** and **PDI$_{assem}$** is statistically significant, judged by the two-tailed *P* value of 0.0363 ($P < 0.05$).

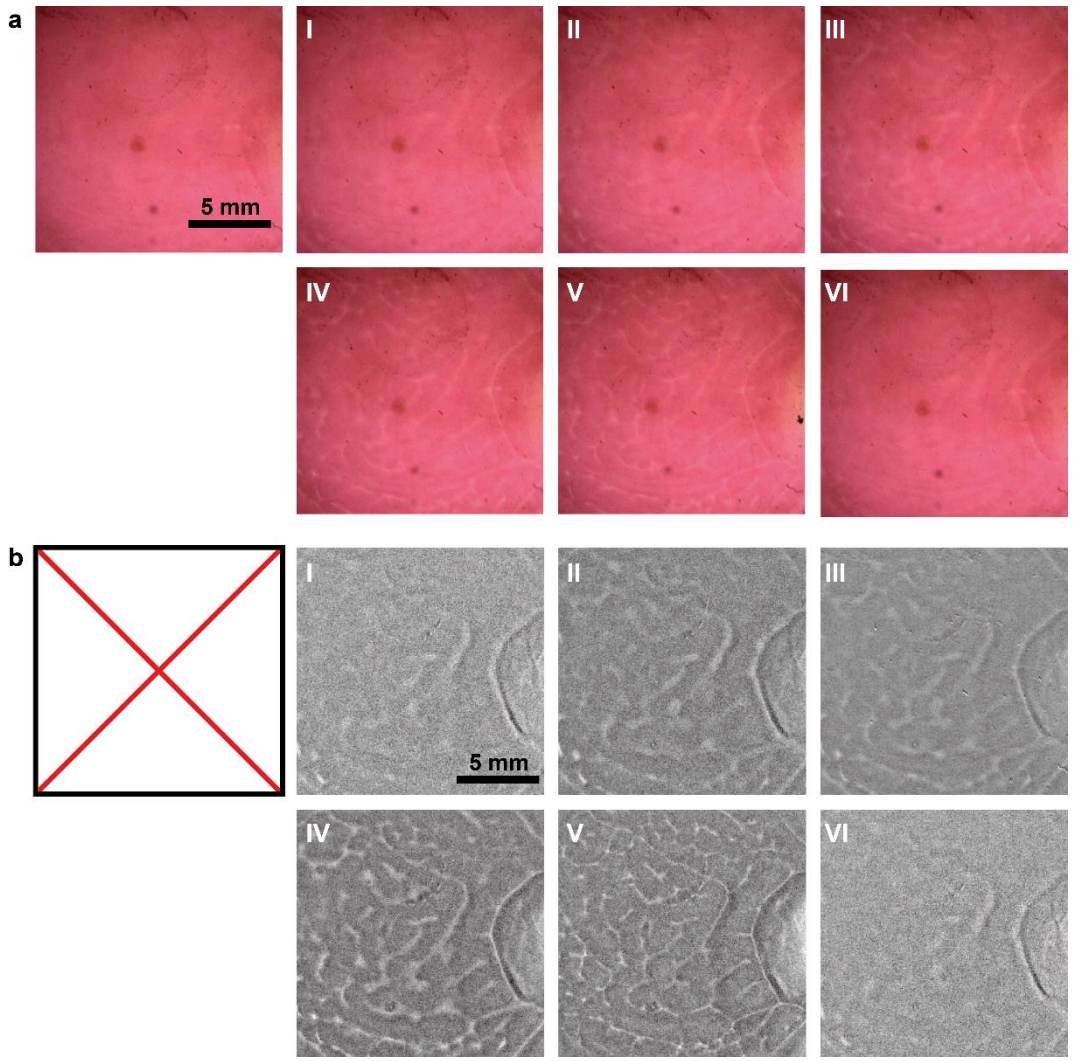

Supplementary Figure 17. Pattern formation. Transient formation of patterns (appearing after ~ 30 min) was observed in a round chip (diameter 12.5 x height 1 mm) while performing propagating front experiments. **a**, Real colour snapshots, **b**, previous snapshots were background corrected by dividing by the initial image (i.e., top left in panel a). Times of the snap shots are: i) 30 min, ii) 33 min, iii) 36 min, iv) 39 min, v) 42 min, vi) 45 min.

Supplementary Section 7. Captions for videos

Supplementary video 1. Supramolecular oscillations in a semi-batch reactor. A **PDI_{mon}** (2.25 mL) solution (75 μM) was recorded under continuous influx of a 400 mM $Na_2S_2O_4$ solution (0.7 μL/min) at constant stirring rate (i.e., 1000 rpm) in a well-ventilated box (constant oxygen supply and light). Colour changes can be observed during supramolecular oscillations between the different assembled (turbid pink colour) and disassembled (clear purple colour) states.

Supplementary video 2. Propagating front of supramolecular assemblies. A freshly oxidized **PDI_{mon}** solution (1.5 mL of a 100 μM **PDI** solution) was immediately injected into the 3D printed chip (50 x 25 x 1 mm). A propagating front in adjacent volumes was observed immediately after addition of **PDI_{assem}** seeds (30 μL of a 1h old **PDI_{mon}** solution) from one side of the chip. Images were acquired using a stereoscope (Nikon SMZ7457) equipped with a CCD camera, frames were recorded every 10 seconds for 60 min. The data shown in Fig. 4b,c corresponds to the video.

Supplementary video 3. The propagating front induces large scale in-plane convection. Large-scale in plane convection was observed in a propagating front experiment. Images were acquired using a ZEISS LSM 710 confocal microscope, frames were recorded every 2 seconds for 30 min. The arrows indicate the direction of the flow and the length is proportional to the speed. The direction and velocity of the flow was tracked using PIVlab tool from Matlab.

Supplementary video 4. Control experiment. Seeded front vs. non-seeded region. A 3D printed chip (45 x 30 mm) was used, which was covered by mineral oil. Buffer solution was added on the left and **PDI_{assem}** seeds on the right of the chip into a freshly oxidized **PDI_{mon}** solution (100 μM, see methods for preparation). Images were acquired using a stereoscope (Nikon SMZ7457) equipped with a CCD camera, frames were recorded every 10 seconds for 50 min.

Supplementary video 5. An outward propagating oxidation front induces flow-alignment of PDI_{assem}. A 3D printed chip (45 x 30 mm) was used, which was covered by mineral oil. **PDI** solution (1.5 mL, filling 3 mm height in the chip) was reduced to **PDI^{2-}** by adding 4 μL of 400 mM $Na_2S_2O_4$ solution. **PDI^{2-}** solution was poured into the chip and carefully covered with mineral oil. An outward moving propagating oxidation front and convection through the entire cell was observed. In addition, **PDI_{assem}** structures aligned along the flow lines. Images were acquired using a stereoscope (Nikon SMZ7457) equipped with a CCD camera, frames were recorded every 10 seconds for 100 min. The data shown in Fig. 4d corresponds to the video.

Supplementary References

1. Leira-Iglesias, J., Sorrenti, A., Sato, A., A. Dunne, P. & M. Hermans, T. Supramolecular pathway selection of perylenediimides mediated by chemical fuels. *Chem. Commun.* **52,** 9009–9012 (2016).

2. Kulkarni, C., Meijer, E. W. & Palmans, A. R. A. Cooperativity Scale: A Structure–Mechanism Correlation in the Self-Assembly of Benzene-1,3,5-tricarboxamides. *Acc. Chem. Res.* **50**, 1928-1936 (2017).

3. Meisl, G. *et al.* Molecular mechanisms of protein aggregation from global fitting of kinetic models. *Nat. Protoc.* **11,** 252–272 (2016).

4. Cohen, S. I. A. *et al.* Nucleated polymerization with secondary pathways. I. Time evolution of the principal moments. *J. Chem. Phys.* **135,** 065105 (2011).